Appendix E

ANALYTICAL METHODS FOR MODELING REAL-WORLD PHOTONIC QUANTUM TELEPORTATION

E.1 Analytical derivations of expressions

HOM interference visibility

We employ the characteristic function formalism described in Chapter 9 considering the setup shown in Fig. 9.2. For this derivation, we use 7×7 block matrices with 2×2 sub-matrices, with each sub-matrix representing correlations between different optical modes. The first column of the block matrix represents the coherent state mode; the third and fifth columns represent vacuum inputs at the virtual beamsplitters with transmission ζ^2 to account for the mode indistiguishability, the second and sixth columns represent the vacuum inputs at the 50:50 beamsplitter that are mixed with the distinguishable parts of the modes; and the fourth and the seventh columns represent the idler and signal modes of the TMSV state. We first describe the overall state of the system after transmission losses, given by the block covariance matrix,

$$\gamma = \begin{pmatrix} \mathbf{I_{2x2}} & 0 & 0 & 0 & 0 & 0 & 0 \\ 0 & \mathbf{I_{2x2}} & 0 & 0 & 0 & 0 & 0 \\ 0 & 0 & \mathbf{I_{2x2}} & 0 & 0 & 0 & 0 \\ 0 & 0 & 0 & (1+2\eta_i\mu)\mathbf{I_{2x2}} & 0 & 0 & 2\sqrt{\eta_i\eta_s\mu(1+\mu)}\sigma_{\mathbf{3}} \\ 0 & 0 & 0 & 0 & \mathbf{I_{2x2}} & 0 & 0 \\ 0 & 0 & 0 & 0 & 0 & \mathbf{I_{2x2}} & 0 \\ 0 & 0 & 0 & 2\sqrt{\eta_i\eta_s\mu(1+\mu)}\sigma_{\mathbf{3}} & 0 & 0 & (1+2\eta_s\mu)\mathbf{I_{2x2}} \end{pmatrix},$$

where $\sigma_{\mathbf{3}} = \begin{pmatrix} 1 & 0 \\ 0 & -1 \end{pmatrix}$. The displacement vector is $\vec{d} = \sqrt{2}\begin{pmatrix} \mathrm{Re}(\alpha) & \mathrm{Im}(\alpha) & 0 & \dots & 0 \end{pmatrix}^T$, with α already accounting for loss in the coherent state channel. From here, we

apply the mismatch matrix,

$$\begin{pmatrix} \sqrt{\zeta}\,\mathbf{I_{2x2}} & 0 & \sqrt{1-\zeta}\,\mathbf{Z} & 0 & 0 & 0 & 0 \\ 0 & \mathbf{I_{2x2}} & 0 & 0 & 0 & 0 & 0 \\ \sqrt{1-\zeta}\,\mathbf{Z} & 0 & \sqrt{\zeta}\,\mathbf{I_{2x2}} & 0 & 0 & 0 & 0 \\ 0 & 0 & 0 & \sqrt{\zeta}\,\mathbf{I_{2x2}} & \sqrt{1-\zeta}\,\mathbf{Z} & 0 & 0 \\ 0 & 0 & 0 & \sqrt{1-\zeta}\,\mathbf{Z} & \sqrt{\zeta}\,\mathbf{I_{2x2}} & 0 & 0 \\ 0 & 0 & 0 & 0 & 0 & \mathbf{I_{2x2}} & 0 \\ 0 & 0 & 0 & 0 & 0 & 0 & \mathbf{I_{2x2}} \end{pmatrix},$$

and the beam splitting matrix,

$$\frac{1}{\sqrt{2}}\begin{pmatrix} \mathbf{I_{2x2}} & 0 & 0 & \mathbf{Z} & 0 & 0 & 0 \\ 0 & \mathbf{I_{2x2}} & 0 & 0 & \mathbf{Z} & 0 & 0 \\ 0 & 0 & \mathbf{I_{2x2}} & 0 & 0 & \mathbf{Z} & 0 \\ \mathbf{Z} & 0 & 0 & \mathbf{I_{2x2}} & 0 & 0 & 0 \\ 0 & \mathbf{Z} & 0 & 0 & \mathbf{I_{2x2}} & 0 & 0 \\ 0 & 0 & \mathbf{Z} & 0 & 0 & \mathbf{I_{2x2}} & 0 \\ 0 & 0 & 0 & 0 & 0 & 0 & \sqrt{2}\,\mathbf{I_{2x2}} \end{pmatrix},$$

where $\mathbf{Z} = \begin{pmatrix} 0 & -1 \\ 1 & 0 \end{pmatrix}$. This now allows calculation of the twofold coincidence probability,

$$\begin{aligned} p_{\text{2-fold}} = \mathrm{Tr}\big\{\hat{\rho}'\big(1 &- \mathbb{I}_{b_1,b_2,b_3,c} \otimes |0\rangle\langle 0|^{\otimes 3}_{a_1,a_2,a_3} \\ &- \mathbb{I}_{a_1,a_2,a_3,c} \otimes |0\rangle\langle 0|^{\otimes 3}_{b_1,b_2,b_3} \\ &+ \mathbb{I}_c \otimes |0\rangle\langle 0|^{\otimes 6}_{a_1,a_2,a_3,b_1,b_2,b_3}\big)\big\}, \end{aligned} \tag{E.1}$$

and the threefold coincidence probability,

$$\begin{aligned} p_{\text{3-fold}} = \mathrm{Tr}\big\{\hat{\rho}'\big(1 &- \mathbb{I}_{a_1,a_2,a_3,b_1,b_2,b_3} \otimes |0\rangle\langle 0|_c \\ &- \mathbb{I}_{b_1,b_2,b_3,c} \otimes |0\rangle\langle 0|^{\otimes 3}_{a_1,a_2,a_3} \\ &- \mathbb{I}_{a_1,a_2,a_3,c} \otimes |0\rangle\langle 0|^{\otimes 3}_{b_1,b_2,b_3} \\ &+ \mathbb{I}_{b_1,b_2,b_3} \otimes |0\rangle\langle 0|^{\otimes 4}_{a_1,a_2,a_3,c} \\ &+ \mathbb{I}_{a_1,a_2,a_3} \otimes |0\rangle\langle 0|^{\otimes 4}_{b_1,b_2,b_3,c} \\ &+ \mathbb{I}_c \otimes |0\rangle\langle 0|^{\otimes 6}_{a_1,a_2,a_3,b_1,b_2,b_3} \\ &- |0\rangle\langle 0|^{\otimes 7}_{a_1,a_2,a_3,b_1,b_2,b_3,c}\big)\big\}, \end{aligned} \tag{E.2}$$

where the subscripts a_i, b_i, and c, with $i \in \{1, 2, 3\}$, represent the coherent state, idler, and signal modes respectively. Note that the subscripts of the identity matrices

indicate which modes are traced out for a given calculation. Using Eq. 9.14, we calculate

$$\mathrm{Tr}\{\hat{\rho}(\mathbb{I}_{x_1,\ldots,x_m}\otimes|0\rangle\langle 0|^{\otimes n}_{y_1,\ldots,y_n}\} = \frac{2^n}{\sqrt{\det\left(\gamma_{y_1,\ldots,y_n}+\mathbb{I}\right)}}\exp\left(-\vec{d}^{T}_{y_1,\ldots,y_n}(\gamma_{y_1,\ldots,y_n}+\mathbb{I})^{-1}\vec{d}_{y_1,\ldots,y_n}\right),$$

where x_i represents the modes traced out and y_i represents the remaining modes. We now use this expression to calculate each of the terms in Eqs. E.1 and E.2, yielding

$$\begin{aligned} p_{\text{2-fold}}(|\alpha|^2,\mu,\zeta,\eta_i) =& 1+\frac{\exp\left(-|\alpha|^2\right)}{1+\eta_i\mu} \\ &- 4\frac{\exp\left(-|\alpha|^2+\frac{|\alpha|^2(2+(1+\zeta^2)\eta_i\mu)}{4+2\eta_i\mu}\right)}{2+\eta_i\mu}, \end{aligned}$$

and

$$\begin{aligned} p_{\text{3-fold}}(|\alpha|^2,\mu,\zeta,\eta_s,\eta_i) =& \frac{\eta_s\mu}{1+\eta_s\mu}-2\frac{\mathrm{e}^{-\frac{|\alpha|^2/2[1+(1-\zeta^2)\eta_i\mu/2]}{1+\eta_i\mu/2}}}{1+\eta_i\mu/2} \\ &+\frac{\mathrm{e}^{-|\alpha|^2}(1-\eta_i)\eta_s\mu}{(1+\eta_i\mu)(1+\eta_s(1-\eta_s)\mu+\eta_s\mu)} \\ &+2\frac{\mathrm{e}^{-\frac{|\alpha|^2/2[1+(1-\zeta^2)(1-\eta_s)\eta_i\mu/2+\eta_s\mu]}{1+(1-\eta_s)\eta_i\mu/2+\eta_s\mu}}}{1+(1-\eta_s)\eta_i\mu/2+\eta_s\mu}. \end{aligned}$$

Teleportation fidelity

We now consider the setup of Fig. 9.2. Similar to the HOM visibility derivation, we use 14×14 block matrices with 2×2 sub-matrices, with each sub-matrix representing correlations between different optical modes. The first and the eight columns of the block matrices represent the early and late coherent state modes; the fourth, and eleventh columns represent the early and late idler modes; the seventh and fourteenth columns represents the early and late signal mode; and the rest represents the vacuum inputs at the virtual and the 50:50 beamsplitters. Again, the block covariance matrix, $\mathbf{I_{6x6}}\oplus\mathbf{M}$, denotes the state of the system after losses, where

$$\mathbf{M} = \mathbf{I_{11x11}}\otimes\mathbf{I_{2x2}} + 2\mu\left(\eta_s\mathbf{P_s}+\eta_i\mathbf{P_i}\right)\otimes\mathbf{I_{2x2}} + 2\sqrt{\eta_s\eta_i\,\mu(1+\mu)}\,\mathbf{A}\otimes\sigma_{\mathbf{3}},$$

$$\mathbf{P_s} = \mathrm{diag}(1,0,0,0,0,0,1,0,0,0,0), \quad \mathbf{P_i} = \mathrm{diag}(0,0,0,0,0,0,0,0,0,1,1),$$

$$\mathbf{A} = \mathbf{E}_{1,10}+\mathbf{E}_{10,1}+\mathbf{E}_{7,11}+\mathbf{E}_{11,7}, \qquad \sigma_{\mathbf{3}} = \begin{pmatrix}1 & 0\\ 0 & -1\end{pmatrix},$$

and $\mathbf{E}_{j,k}$ is an 11×11 matrix unit at (j,k) and 0 elsewhere.

The displacement vector is,

$$\vec{d} = \sqrt{2}\begin{pmatrix} \mathrm{Re}(\alpha) & \mathrm{Im}(\alpha) & 0 & 0 & 0 & 0 & 0 & 0 & 0 & 0 \\ 0 & 0 & \mathrm{Re}(\alpha) & \mathrm{Im}(\alpha) & 0 & 0 & ... & 0 & & \end{pmatrix}^T,$$

and α again already takes into account loss. The mismatch matrix,

$$\mathbf{I_{2x2}} \otimes \begin{pmatrix} \sqrt{\zeta}\,\mathbf{I_{2x2}} & 0 & \sqrt{1-\zeta}\,\mathbf{Z} & 0 & 0 & 0 \\ 0 & \mathbf{I_{2x2}} & 0 & 0 & 0 & 0 \\ \sqrt{1-\zeta}\,\mathbf{Z} & 0 & \sqrt{\zeta}\,\mathbf{I_{2x2}} & 0 & 0 & 0 \\ 0 & 0 & 0 & \sqrt{\zeta}\,\mathbf{I_{2x2}} & \sqrt{1-\zeta}\,\mathbf{Z} & 0 \\ 0 & 0 & 0 & \sqrt{1-\zeta}\,\mathbf{Z} & \sqrt{\zeta}\,\mathbf{I_{2x2}} & 0 \\ 0 & 0 & 0 & 0 & 0 & \mathbf{I_{2x2}} \end{pmatrix} \oplus \mathbf{I_{4x4}},$$

is applied, and so is the beam splitting matrix,

$$\frac{1}{\sqrt{2}}\mathbf{I_{2x2}} \otimes \begin{pmatrix} \mathbf{I_{2x2}} & 0 & 0 & \mathbf{Z} & 0 & 0 \\ 0 & \mathbf{I_{2x2}} & 0 & 0 & \mathbf{Z} & 0 \\ 0 & 0 & \mathbf{I_{2x2}} & 0 & 0 & \mathbf{Z} \\ \mathbf{Z} & 0 & 0 & \mathbf{I_{2x2}} & 0 & 0 \\ 0 & \mathbf{Z} & 0 & 0 & \mathbf{I_{2x2}} & 0 \\ 0 & 0 & \mathbf{Z} & 0 & 0 & \mathbf{I_{2x2}} \end{pmatrix} \oplus \mathbf{I_{4x4}}.$$

The above result is in the Z-basis. For the X-basis, we apply the phase shift matrix to the early signal mode,

$$\mathbf{I_{12x12}} \oplus \begin{pmatrix} \cos(\phi) & \sin(\phi) \\ -\sin(\phi) & \cos(\phi) \end{pmatrix} \oplus \mathbf{I_{14x14}},$$

and then interfere the early and late signal mode at a 50:50 beamsplitter, described by the matrix,

$$\mathbf{I_{12x12}} \oplus \begin{pmatrix} \frac{1}{\sqrt{2}}\mathbf{I_{2x2}} & 0 & 0 & 0 & 0 & 0 & 0 & \frac{1}{\sqrt{2}}\mathbf{Z} \\ 0 & \mathbf{I_{2x2}} & 0 & 0 & 0 & 0 & 0 & 0 \\ 0 & 0 & \mathbf{I_{2x2}} & 0 & 0 & 0 & 0 & 0 \\ 0 & 0 & 0 & \mathbf{I_{2x2}} & 0 & 0 & 0 & 0 \\ 0 & 0 & 0 & 0 & \mathbf{I_{2x2}} & 0 & 0 & 0 \\ 0 & 0 & 0 & 0 & 0 & \mathbf{I_{2x2}} & 0 & 0 \\ 0 & 0 & 0 & 0 & 0 & 0 & \mathbf{I_{2x2}} & 0 \\ \frac{1}{\sqrt{2}}\mathbf{Z} & 0 & 0 & 0 & 0 & 0 & 0 & \frac{1}{\sqrt{2}}\mathbf{I_{2x2}} \end{pmatrix},$$

before the detection. In both the X- and Z-basis, we calculate the relevant threefold detection probabilities as follows:

$$\begin{aligned} P_{D_1D_4D_6} = \mathrm{Tr}\{\hat{\rho}'(1 &- \mathbb{I}_{a_l,b_e,b_l,c_e,c_l} \otimes |0\rangle\langle 0|_{a_e}^{\otimes 3} - \mathbb{I}_{a_e,a_l,b_e,c_e,c_l} \otimes |0\rangle\langle 0|_{b_l}^{\otimes 3} \\ &- \mathbb{I}_{a_e,a_l,b_e,b_l,c_e} \otimes |0\rangle\langle 0|_{c_l} + \mathbb{I}_{a_l,b_e,b_l,c_e} \otimes |0\rangle\langle 0|_{a_e,c_l}^{\otimes 4} \\ &+ \mathbb{I}_{a_e,a_l,b_e,c_e} \otimes |0\rangle\langle 0|_{b_l,c_l}^{\otimes 4} + \mathbb{I}_{a_l,b_e,c_e,c_l} \otimes |0\rangle\langle 0|_{a_e,b_l}^{\otimes 6} \\ &- \mathbb{I}_{a_l,b_e,c_e} \otimes |0\rangle\langle 0|_{a_e,b_l,c_l}^{\otimes 7})\}, \end{aligned} \tag{E.3}$$

where the subscripts a, b, and c represent the coherent state, idler, and signal modes respectively, and the subscripts e and l represent the early or late bin, respectively. Again, the subscripts of the identity matrix indicate which modes are traced out for a given calculation. Similarly as before, we use Eq. 9.14 to calculate each of the terms in Eq. E.3 to yield analytical expressions of the probabilities.

E.2 Maximum theoretical HOM interference visibilities

We plot the maximum two- and three-fold interference HOM interference visibilities using Eqs. 9.18 and 9.19. Complete indistinguishability $\zeta = 1$ as well as perfect transmission $\eta_s = \eta_i = 1$ is assumed. The visibilities with varied $|\alpha|^2$ and μ are shown in Fig. E.1, finding maximum two- and three-fold visibilities of $\sqrt{2} - 1$ and unity, respectively.

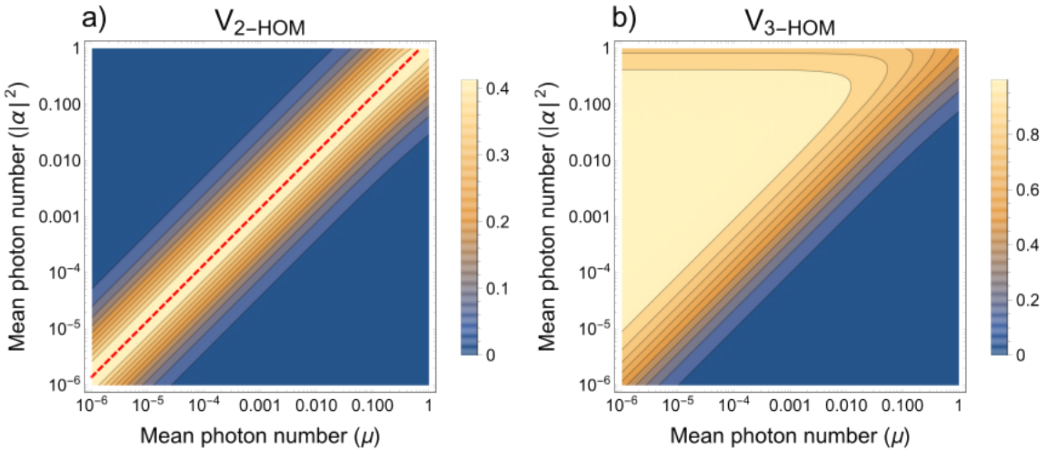

Figure E.1: Dependence of a) two-fold and b) three-fold HOM interference visibilities for varied mean photon numbers of the coherent state ($|\alpha|^2$) and TMSV (μ) assuming unity path efficiencies ($\eta_i, \eta_s = 1$) and photon indistinguishability ($\zeta = 1$). The red dashed line in a) corresponds to $|\alpha|^2 = \sqrt{2}\mu$, which maximizes the visibility for $|\alpha|^2, \mu \ll 1$.

The two-fold plot features a maximum along a symmetric diagonal for all $|\alpha|^2 \ll 1$ and $\mu \ll 1$. The maximum corresponds to the condition $|\alpha|^2/\mu = \sqrt{2}$, which is not equal to one due to the differences in number distributions. This condition effectively corresponds to matching of the mean photon numbers of the Poisson and thermal distributions, 'striking a balance" between the contributions of single photons interfering compared to $n = 2$ terms interfering with vacuum. Thus, the $\sqrt{2}$ acts to ensure that the balance is struck between the different field statistics. This is different than the case of identical field statistics, in which the maximum corresponds to an exact matching of mean photon numbers. Note the slight deviation in diagonal symmetry as $|\alpha|$ and μ approach 1; the balancing offered by $\sqrt{2}$ cannot hold because interference between single and $n = 2$ states begin to contribute to interference. Indeed the maximum visibility is not unity due to the non-zero contribution of $n = 2$ terms interfering with vacuum.

Owing to heralding, the three-fold plot has a plateau-like topography that extends the range of optimized visibility. A range of $|\alpha|^2 \ll 1$ will maximize the visibility to approach unity because the measurement is conditioned on three-fold detection and heralding will always guarantee a single photon in the idler mode when $\mu \ll 1$. Effectively, this regime renders the visibility independent of the probability of generating a photon in $|\alpha\rangle$. The threshold at $|\alpha|^2 \sim 1$ is predominantly due to $n = 2$ events from $|\alpha\rangle$ interfering with heralded single photons in the idler path, thereby reducing the maximum visibility. A steep diagonal threshold to the plateau is also present under conditions of $|\alpha|^2 \ll 1$, similar to that of the ridge in the two-fold plot. In this region, as μ is increased and approaches $|\alpha|^2$, the relative probability of heralding a multi-photon term increases, which decreases the visibility, and leads to the threshold topography along the diagonal. The condition $|\alpha|^2/\mu = \sqrt{2}$ does not maximize the visibility because heralding increases the effective mean photon number of the signal mode, and thus a lower value of μ is required to reach maximum visibility compared to two-fold HOM interference. This effect shifts the diagonal threshold to the left in Fig. E.1b.

E.3 Procedure for fitting HOM interference and teleportation fidelity datasets

We fit three data sets, two- and three-fold HOM interference visibilities as well as X-basis teleportation fidelity, using a piecewise model function based on our theory. Our code performs a nonlinear regression with Mathematica's `NonlinearModelFit` function with Differential Evolution as the fitting method. This global optimization approach is well-suited for fitting nonlinear models. As discussed in Sec. 9.4, we

utilize six physical parameters: η_s, η_{i2}, η_{i3}, μ, ζ_2, and ζ_3, as fitting parameters, subject to relevant physical constraints. Different mode mismatch and signal mode efficiency parameters, ζ_2 and ζ_3, as well as η_{i2} and η_{i3}, respectively, are ascribed to the two- and three-fold detection experiments. For the three-fold HOM and teleportation data, a shared ζ_3 is used, with independently determined parameters $\eta_{i3} = 1.2 \times 10^{-2}$, $\eta_s = 4.5 \times 10^{-3}$, and $\mu = 8.0 \times 10^{-3}$ from Ref. [1] remaining constant. The two-fold HOM data is fitted independently, retaining $\mu = 8.0 \times 10^{-3}$ as constant.

The fitting protocol is outlined as follows:

1. Use the `Map` and `Max` functions to ensure uncertainties in the data are bounded to be no less than the square root of the respective y-values.

2. Combine the three-fold HOM interference and X-basis visibility data, distinguishing them with unique markers. This is achieved using the `Join` and `Map` functions.

3. Formulate a modular fitting function, which can differentiate between X-basis visibility and three-fold HOM interference based on their respective markers. For two-fold HOM data, introduce a separate fitting function that considers the unique constraints of the two-fold detection experiment.

4. Establish the fitting framework, setting the fitting parameters such as η_{i2}, ζ_2, and ζ_3 accordingly, while holding the known parameters constant.

5. Engage in a simultaneous fitting procedure using `NonlinearModelFit`. This process will take into account the defined model function constraints, weigh the data points based on their squared uncertainties, and adopt the "DifferentialEvolution" fitting technique. The physical constraints on the fitting parameters will ensure that path efficiencies and indistinguishabilities are positive and no larger than unity.

The outcomes of the fits yield $\zeta_2 = 0.80 \pm 0.04$, $\eta_{i2} = (6.9 \pm 1.2) \times 10^{-2}$, and $\zeta_3 = 0.90 \pm 0.02$ as optimal parameter estimations.

E.4 Calculus of HOM interference visibility expressions

We differentiate the HOM visibility expressions of Eqs. 9.18 and 9.19 to determine the optimal choice of $|\alpha|^2$. The expression for the two-fold case (Eq. 9.18), when

differentiated with respect to $|\alpha|^2$ and evaluated for the relevant experimental and extracted parameters $\zeta_2 = 0.80$, $\eta_i = 6.9 \times 10^{-2}$ and $\mu = 8.0 \times 10^{-3}$, yields,

$$V'_{\text{2-HOM}}(|\alpha|^2) = \frac{-1.98781e^{|\alpha|^2/2} - 55552.9e^{0.500019|\alpha|^2} + 55554.9e^{0.500019|\alpha|^2}}{0.987811 - 1.98781e^{|\alpha|^2/2} + e^{|\alpha|^2}}. \tag{E.4}$$

The three-fold case (Eq. 9.19), given a similar treatment with $\zeta_3 = 0.90$, $\eta_i = 1.2 \times 10^{-2}$, $\eta_s = 4.5 \times 10^{-3}$ and $\mu = 8.0 \times 10^{-3}$, yields

$$\begin{aligned} V'_{\text{3-HOM}}(|\alpha|^2) = \frac{1}{\left(0.987811 - 1.98781e^{|\alpha|^2/2} + e^{|\alpha|^2}\right)^2}\Big[&-0.98179e^{|\alpha|^2/2} \\ &- 27439.2e^{0.500024|\alpha|^2} + 27440.2e^{0.500024|\alpha|^2} \\ &+ 2.22045 \times 10^{-16}e^{|\alpha|^2} + 2.63814e^{1.00002|\alpha|^2} \\ &- 2.65025e^{1.00002|\alpha|^2} + 0.993905e^{3|\alpha|^2/2} \\ &+ 27775.1e^{1.50002|\alpha|^2} - 27776.1e^{1.50002|\alpha|^2}\Big] \end{aligned} \tag{E.5}$$

Setting Eqs. E.4 and E.5 equal to zero and evaluating $|\alpha|^2$ results in 7.8×10^{-4} and 2.2×10^{-3}, respectively, which is consistent with the curves shown in Fig. 9.3.

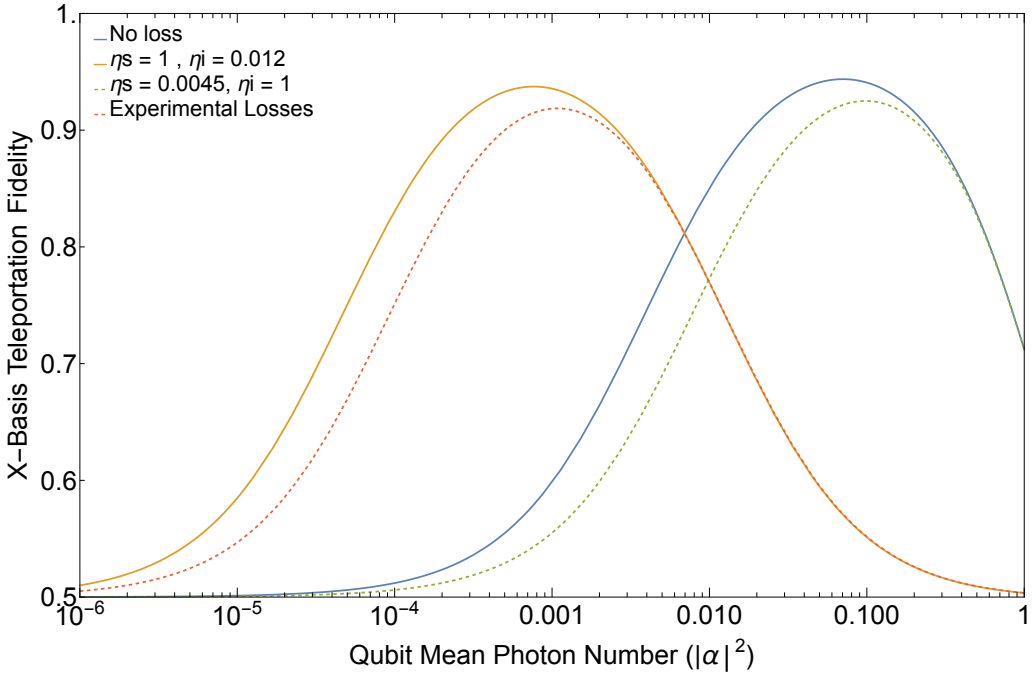

Figure E.2: Model of teleportation fidelity of X-basis states for varied $|\alpha|^2$ under conditions of varied signal and idler transmission efficiencies in blue, red, green, and orange, respectively, as described in Sec. 9.5 the main text, assuming complete indistinguishability $\zeta = 1$.

E.5 X-basis teleportation curves for varying transmission efficiencies and mean photon numbers

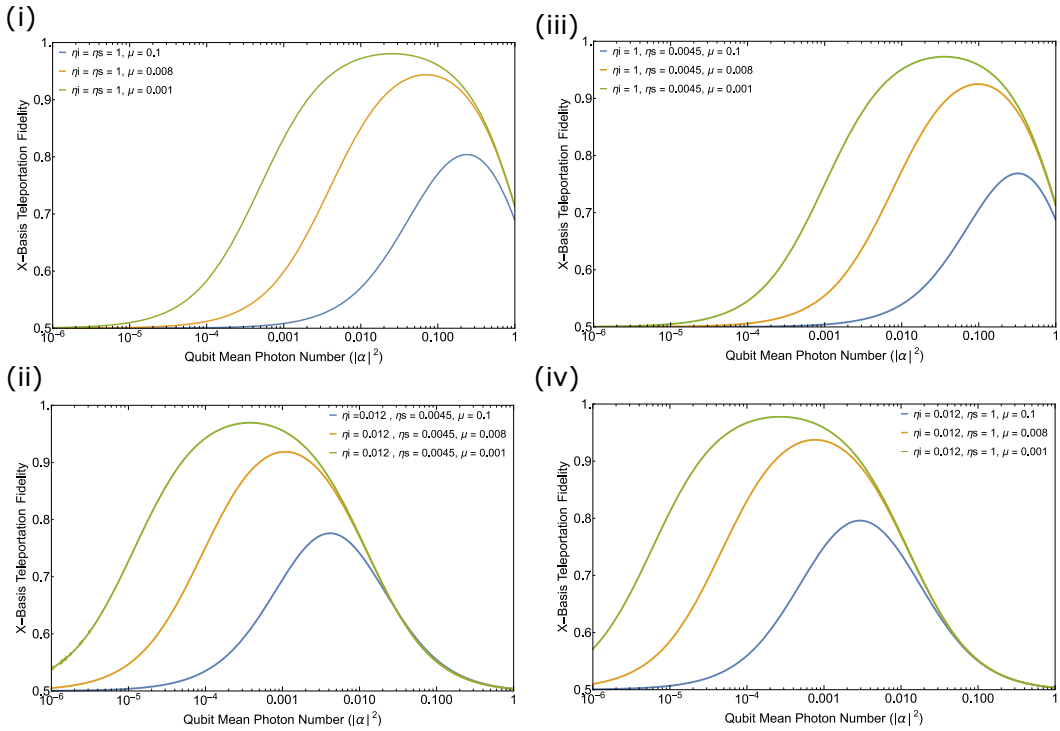

Figure E.3: Model of X-basis quantum teleportation fidelity for varied $|\alpha|^2$ and $\mu < 10^{-2}$, under varied signal and idler transmission efficiencies cases (i)-(iv), as discussed in Sec. 9.5, assuming complete indistinguishability $\zeta = 1$.

References

[1] Raju Valivarthi, Samantha I. Davis, Cristián Peña, et al. "Teleportation Systems Toward a Quantum Internet." In: PRX Quantum 1 (2 Dec. 2020), p. 020317. DOI: 10.1103/PRXQuantum.1.020317. URL: https://link.aps.org/doi/10.1103/PRXQuantum.1.020317.